SOFT ROBOTS

Scale-inspired programmable robotic structures with concurrent shape morphing and stiffness variation

Tianyu Chen, Xudong Yang, Bojian Zhang, Junwei Li, Jie Pan, Yifan Wang*

Biological organisms often have remarkable multifunctionality through intricate structures, such as concurrent shape morphing and stiffness variation in the octopus. Soft robots, which are inspired by natural creatures, usually require the integration of separate modules to achieve these various functions. As a result, the whole structure is cumbersome, and the control system is complex, often involving multiple control loops to finish a required task. Here, inspired by the scales that cover creatures like pangolins and fish, we developed a robotic structure that can vary its stiffness and change shape simultaneously in a highly integrated, compact body. The scale-inspired layered structure (SAILS) was enabled by the inversely designed programmable surface patterns of the scales. After fabrication, SAILS was inherently soft and flexible. When sealed in an elastic envelope and subjected to negative confining pressure, it transitioned to its designated shape and concurrently became stiff. SAILS could be actuated at frequencies as high as 5 hertz and achieved an apparent bending modulus change of up to 53 times between its soft and stiff states. We further demonstrated both the versatility of SAILS by developing a soft robot that is amphibious and adaptive and tunable landing systems for drones with the capacity to accommodate different loads.

INTRODUCTION

In biological systems, sophisticated multifunctionality emerges from intricate yet highly integrated structures (*1*, *2*). Organisms in both plants (*3*) and animals (*4*) often showcase remarkable abilities to alter their shape and adjust their stiffness concurrently in response to dynamic environmental conditions. As an emerging field, soft robotics has been substantially inspired by these biological systems to achieve high flexibility and environmental adaptability (*5*, *6*). Moreover, soft robots are being increasingly considered as viable assistants for humans across diverse fields—from industrial operations to search and rescue and health care (*7*–*11*). Unlike their rigid counterparts, soft robots exhibit the potential to integrate and interact in human-centric environments, primarily because of their inherent compliance and capacity to execute tasks in a safe manner (*12*). However, because soft robots are mainly composed of soft materials such as silicone elastomer (*13*, *14*), they have a very limited load-carrying capacity and structural rigidity. To address this shortcoming, various variable-stiffness mechanisms have been proposed (*15*, *16*), such as antagonistic actuation (*17*–*19*), the use of magnetorheological fluid (*20*) or low-melting point alloys (*21*, *22*), and material jamming (*23*–*25*). In contrast with highly integrated biological organisms, a common issue with these solutions is that either several actuators need to be combined together and controlled coordinately (*17*–*19*) or the variable-stiffness modules need to be integrated with additional actuation modules for shape change (*26*, *27*). These integrations of separate modules will ultimately lead to a bulky overall device with poor manufacturing scalability (*28*, *29*) and a complicated, multistep control system (*25*, *30*, *31*). Although these integrations can offer greater system flexibility, allowing independent control of stiffness and shape, there are scenarios where these functions are pursued together, such as in medical devices (*32*) or deployable structures (*33*). Therefore, it is highly desirable to create a robotic structure with an integrated body that uses one control loop to achieve programmed actuation and stiffness variation simultaneously.

Reflecting on nature's remarkable solutions to such challenges, we observed creatures cloaked in scales, such as pangolins (Manidae) and fish. Their scaled surfaces are exquisite examples of how evolution has provided a synergistic adaptation between flexibility and rigidity (*34*–*38*). The scaled structure has inspired the development of several flexible armors (*38*–*40*) and variable-stiffness structures (*41*, *42*), which directly take advantage of the unique mechanical properties of a scaled structure. Moreover, a scaled structure can serve as a skeleton for integrating multifunctional capabilities, such as embodied energy (*43*), remote biomedical heating (*44*), and microwave absorption (*45*).

In this work, we present the scale-inspired layered structure (SAILS), a soft robotic structure inspired by the variable stiffness of biological organisms and the unique mechanical properties of and multifunctional integration in natural scaled structures. SAILS uniquely combines shape-morphing and variable-stiffness capabilities in a cohesive framework. Composed of a base layer with multiple scales, as illustrated in Fig. 1, SAILS is characterized by its programmed surface patterns. By enclosing SAILS in a sealed envelope and applying negative pressure, the surface patterns on the scales and the base layer are compressed and coupled together, resulting in the whole structure morphing into a predetermined shape while simultaneously gaining higher rigidity (a 52-fold increase in the apparent bending modulus). Because SAILS uses negative instead of positive pressure for actuation, with pressure changes below 1 atm, it has a relatively high actuation frequency (up to 5 Hz), and actuation does not inflate its volume. Because of this feature, the robotic structure can be fabricated and remain as thin as ~1 mm, with the potential for further scaling down. We demonstrate the versatility of our design through two practical applications: a soft amphibious robot that could complete a series of tasks—including ground crawling, swimming, slope climbing, narrow channel passing, obstacle overcoming, and load bearing—and a drone landing gear adaptable to varying loads for protection. With these examples, we aim to

---

School of Mechanical and Aerospace Engineering, Nanyang Technological University, 50 Nanyang Avenue, 639798 Singapore.
*Corresponding author. Email: yifan.wang@ntu.edu.sg

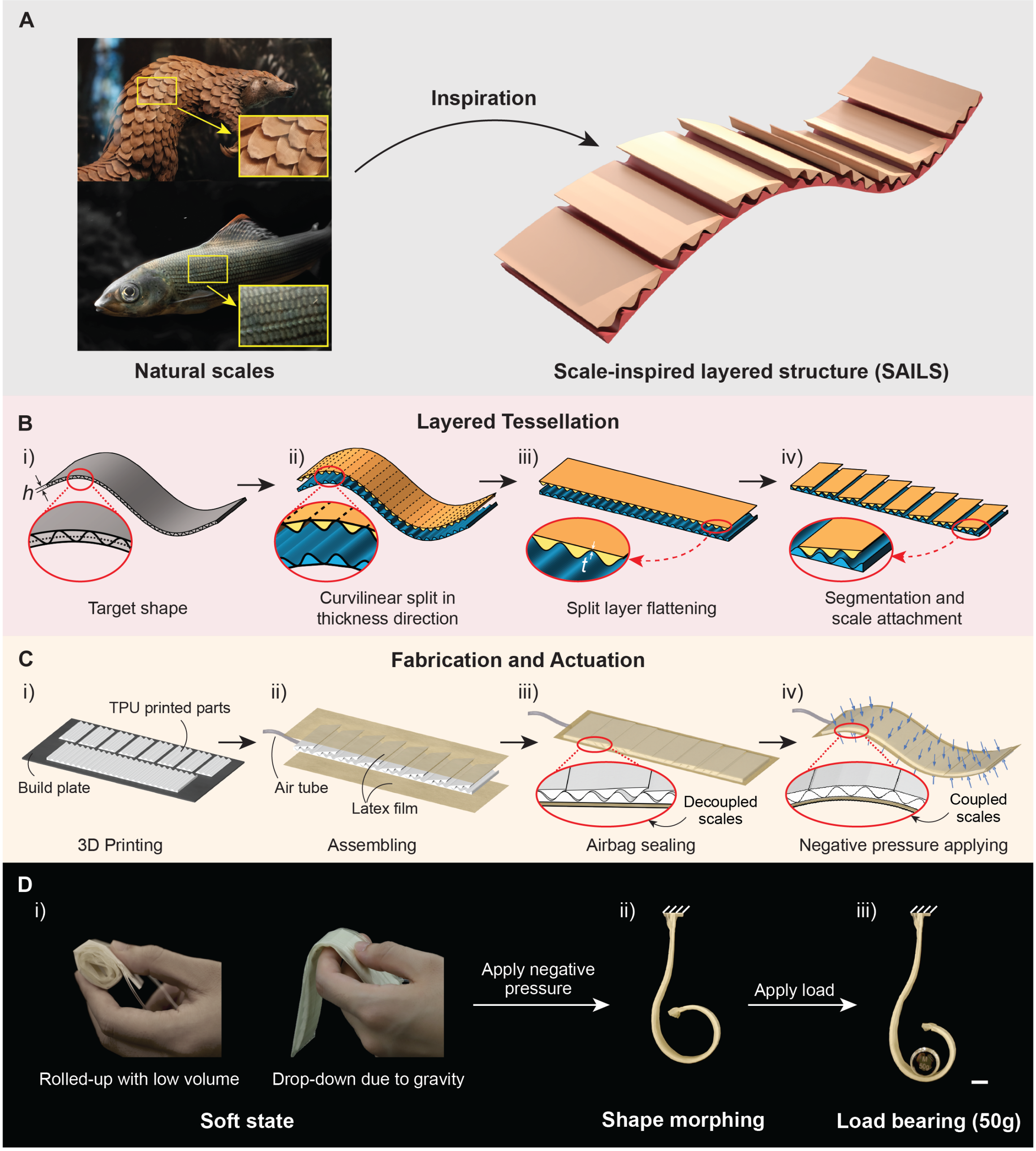

Fig. 1. Bioinspiration, design, fabrication, and experimental validation of SAILS. (**A**) SAILS inspired by the natural scales of pangolins and fish with a designed surface pattern. (**B**) The layered tessellation for generating the surface pattern on the scales and the base layer of SAILS. (**C**) The fabrication and actuation process of SAILS, including 3D printing of the parts; assembling the 3D-printed parts, latex film, and air tube; sealing of the two films to form an airbag; and applying negative pressure to the assembled structure. (**D**) Experimental validation of the shape-morphing and variable-stiffness capabilities of SAILS. The negative pressure is 90 kPa. Scale bar, 2 cm.

create opportunities for future soft robots that are highly integrated and mimic multifunctional biological organisms.

RESULTS

Design and fabrication of SAILS

The bioinspiration, design, fabrication, and experimental validation of SAILS are shown in Fig. 1. We used a top-down approach, termed layered tessellation, to generate the surface patterns on the scales and the base layer, which is illustrated in Fig. 1B. Here, a target shape with a wave-like profile and a thickness h was used as an example to elucidate this process. First, the middle surface of the target shape was identified [represented by the dashed line in Fig. 1B (i)]. Second, a sinusoidal curved cutting surface with an amplitude of $h/2$ and a specified number of periods was drawn along the middle surface, separating the plate into two parts, colored blue and orange, respectively. The upper and lower surfaces of the separated layers were then discretized into quadrilaterals, with their edges indicated by the dashed lines in Fig. 1B (ii). Third, the separated upper and lower layers were flattened by rotating the angles between each discrete unit while maintaining the unit geometry, such that the lower and upper boundaries both became flat surfaces, as shown in Fig. 1B (iii). Then, a thin supporting sheet with thickness t was added to the back of each layer to enhance the mechanical strength after the layers were manufactured, as depicted in the inset of Fig. 1B (iii). Last, the upper layer was divided into several segments, namely scales, to ensure that each period in the surface patterns on the scales matches the corresponding one on the base layer when the entire sample is laid flat. Otherwise, substantial mismatches of the patterns over too many periods would result in a deformed shape deviating from the desired target. The scales were then attached to the base layer to form SAILS, as shown in Fig. 1B (iv) (see Supplementary Methods for the mathematical description of the layered tessellation process).

The fabrication and actuation process of SAILS is demonstrated in Fig. 1C and movie S1. The fabrication details are described in Materials and Methods. First, the scales and the base layer were fabricated with a fused deposition modeling (FDM) three-dimensional (3D) printer using thermoplastic polyurethane (TPU) filament [Fig. 1C (i)]. The scales and the base layer were then coated with a layer of polytetrafluoroethylene (PTFE) tape to reduce the friction during actuation. Then, the scales were selectively heated on one side to adhere to the base layer using an electric soldering iron. Subsequently, SAILS was encased in two pieces of latex film, each 0.1 mm thick, which were then sealed together using silicone glue, forming an air-tight envelope [Fig. 1C (ii) and (iii)]. A soft tube was also attached to the envelope to control the internal pressure. At this point, the scales and the base layer remained decoupled [inset of Fig. 1C (iii)], leaving the entire structure soft and pliable. On completion of the assembly, SAILS could be actuated by applying negative pressure through the soft tube, as illustrated in Fig. 1C (iv). This caused the surface patterns on the scales and the base layer to be compressed and coupled together [inset of Fig. 1C (iv)], enabling the structure to morph into the target shape and simultaneously become stiff.

After fabrication, the concurrent shape-morphing and stiffness-variation process of SAILS was experimentally demonstrated, as shown in Fig. 1D. When no negative pressure was applied, very little coupling existed between the base layer and the scales. As a result, the structure was soft and flexible, allowing it to be compactly rolled up or to sag under the influence of gravity [Fig. 1D (i)]. With the application of a negative pressure of 90 kPa, namely, equivalent to −90 kPa relative to atmospheric pressure (a convention followed for all negative pressure values reported here), the structure underwent a transformation to assume a predesigned hook-like shape [Fig. 1D (ii)], demonstrating its shape-morphing capability. Moreover, the structure stiffness increased notably during this morphing process. The structure was able to hold a 50-g weight [Fig. 1D (iii)], showcasing its increased rigidity.

Shape morphing of SAILS

To demonstrate the shape-morphing capability of SAILS, we showcased several typical structures with developable surfaces, namely, surfaces that can be flattened without distortion and have zero Gaussian curvature, realized by SAILS in Fig. 2 and movie S2. The dimensions of the shapes are detailed in fig. S1. The negative pressure used in the simulations and experiments was 90 kPa. We compared the target shapes, the finite element (FE) simulations (see Materials and Methods for details), and the experimental results, which were all in good agreement, with the root mean square error (RMSE) within ~5% for structures with developable surfaces (see Supplementary Methods for details). First, we showed a hook-shaped surface characterized by an increasing curvature from the fixed end to the free end (Fig. 2, A to D). Second, we demonstrated a wave-shaped surface (Fig. 2, E to H). Third, a helix-shaped surface in which the surface pattern orientation had an angle of 70.62° with respect to the front surface instead of the 90° in previous designs is depicted in Fig. 2 (I to L). The results for two additional spline-based developable surfaces are shown in fig. S2. The design parameters for these structures are listed in table S1.

In addition to these geometries with zero Gaussian curvatures, structures with nondevelopable surfaces, which have nonzero Gaussian curvatures, are presented in Fig. 2 (M to T). Because SAILS could only bend in one direction, meshed configurations were used. Because of the interaction between grid lines in different directions, each mesh segment cannot fully realize its designed shape. As a result, we could only approximate the nondevelopable surfaces, with an RMSE of ~10% between the FE simulation and the target. We first showed a dome-shaped surface with a positive Gaussian curvature in Fig. 2 (M to P), in which we used a three-by-three mesh with each row/column deformed toward a half-circle shape (fig. S1). We then designed a saddle-shaped surface with a negative Gaussian curvature in Fig. 2 (Q to T). The same three-by-three mesh was used as that shown in Fig. 2N with the exception that three columns in the y direction were flipped upside down (see inset in Fig. 2R) such that the bending directions were opposite in the x and y directions. The Gaussian curvature distributions of the two target surfaces are shown in fig. S3. We further demonstrated the deployment process of the structure with a dome-shaped surface built on SAILS (Fig. 2U, movie S3, and Supplementary Methods), which can withstand a load of 50 g, more than four times its own weight (12 g without tube).

To quantitatively evaluate the shape-morphing capability of SAILS, we fabricated a SAILS that had a target shape of a circle with a radius of 15.92 mm, corresponding to a perimeter of 10 cm and a curvature of 0.0628 mm^{-1}. We then recorded the shapes of SAILS under various negative pressures ranging from 0 to 90 kPa and plotted them in Fig. 3A. The sample, with four scales each having three periods, had dimensions of 2 mm in thickness and 3 cm in width. For comparison, the results from FE simulations were also included, demonstrating good agreement with the experimental observation. We further calculated the curvatures of the shapes from Fig. 3A and compared them in Fig. 3B. The results show that the curvature of SAILS progressively approached the target curvature with increasing negative pressures. As the negative pressure increased to 90 kPa, the curvature of SAILS reached 0.0534 mm^{-1}, which was very close to the target curvature (represented by the red dashed line in Fig. 3B). The stress and strain distributions of SAILS and the airbag under a negative pressure of 90 kPa (fig. S4) indicate that the stress and strain concentration primarily occurred at the thinnest regions of both the scales and the base layer. In addition, we observed a higher stress and strain level at the interfaces where the scales and base layer are in contact. In contrast, the bulk of SAILS experienced a substantially lower stress level (typically below 0.1 MPa) and strain level (under 0.1%). In addition, the maximum true strain observed in the airbag was 1.32, equating to an engineering strain of 2.74. This figure is notably below the stretching limit of the latex film, which can extend up to seven times its original length.

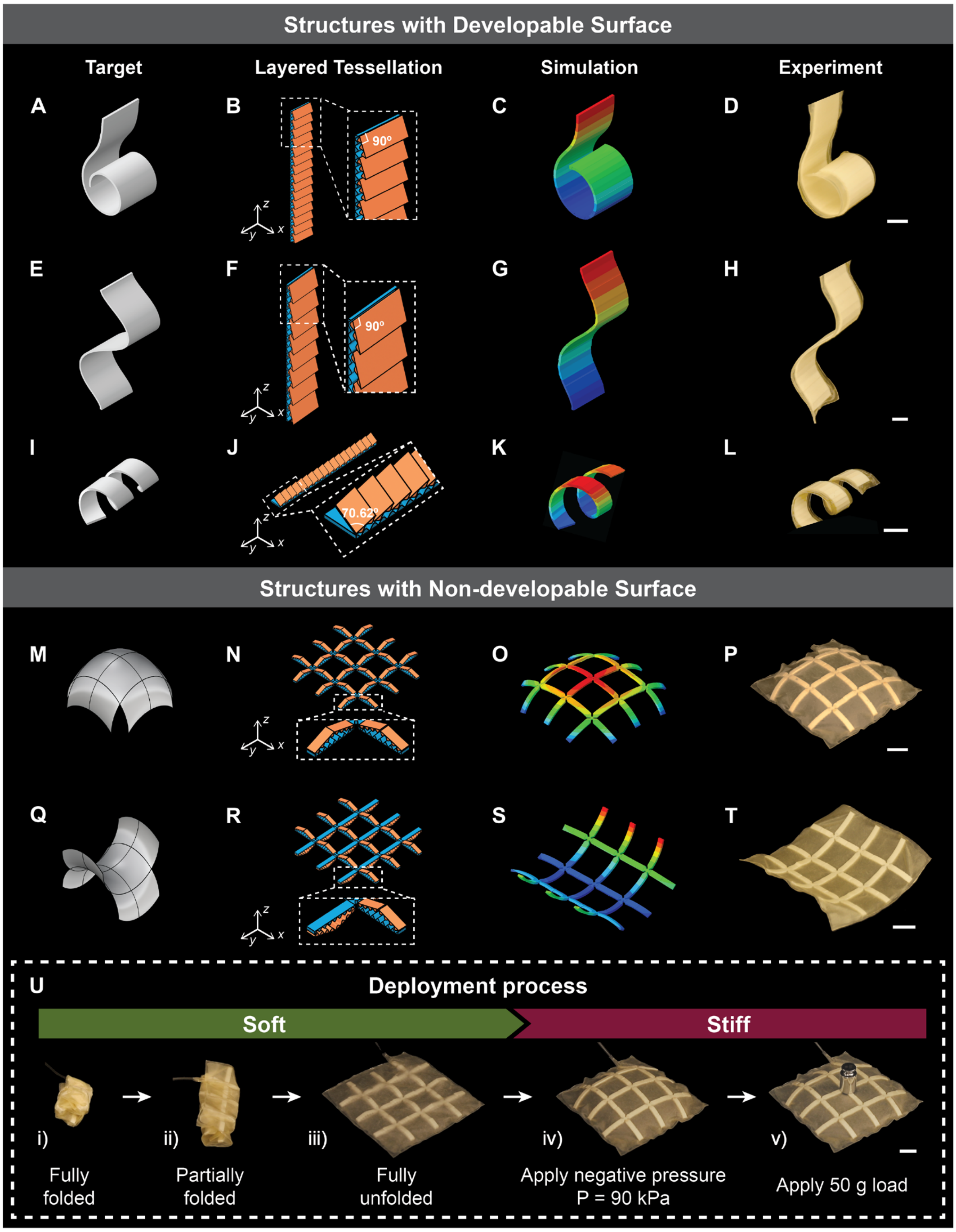

Fig. 2. Various structures with developable and nondevelopable surfaces achieved by SAILS. Target shape, layered tessellation, FE simulation, and experimental results of structures with developable (**A** to **D**) hook-shaped, (**E** to **H**) wave-shaped, and (**I** to **L**) helix-shaped surfaces, along with nondevelopable (**M** to **P**) dome-shaped and (**Q** to **T**) saddle-shaped surfaces. The detailed dimensions of the target shapes are given in fig. S1. (**U**) Deployment process of the dome-shaped surface. Scale bar, 2 cm.

Stiffness variation of SAILS

To quantitatively characterize the stiffness variation of SAILS under negative pressure, we measured force-deflection curves of SAILS under three-point bending tests at six negative pressure levels ranging from 0 to 90 kPa (Fig. 3C). The setup of the experiment is described in Materials and Methods. The SAILS samples used for these tests had a length of 10 cm, a width of 3 cm, and a thickness of 2 mm. In the test, as depicted in the inset of Fig. 3C, the sample consisted of four scales, each comprising three periods. We fabricated two samples and tested each three times to obtain the average force-deflection curves. The shaded area in Fig. 3C represents the SD. The results showed that the stiffness of the structure increased monotonically

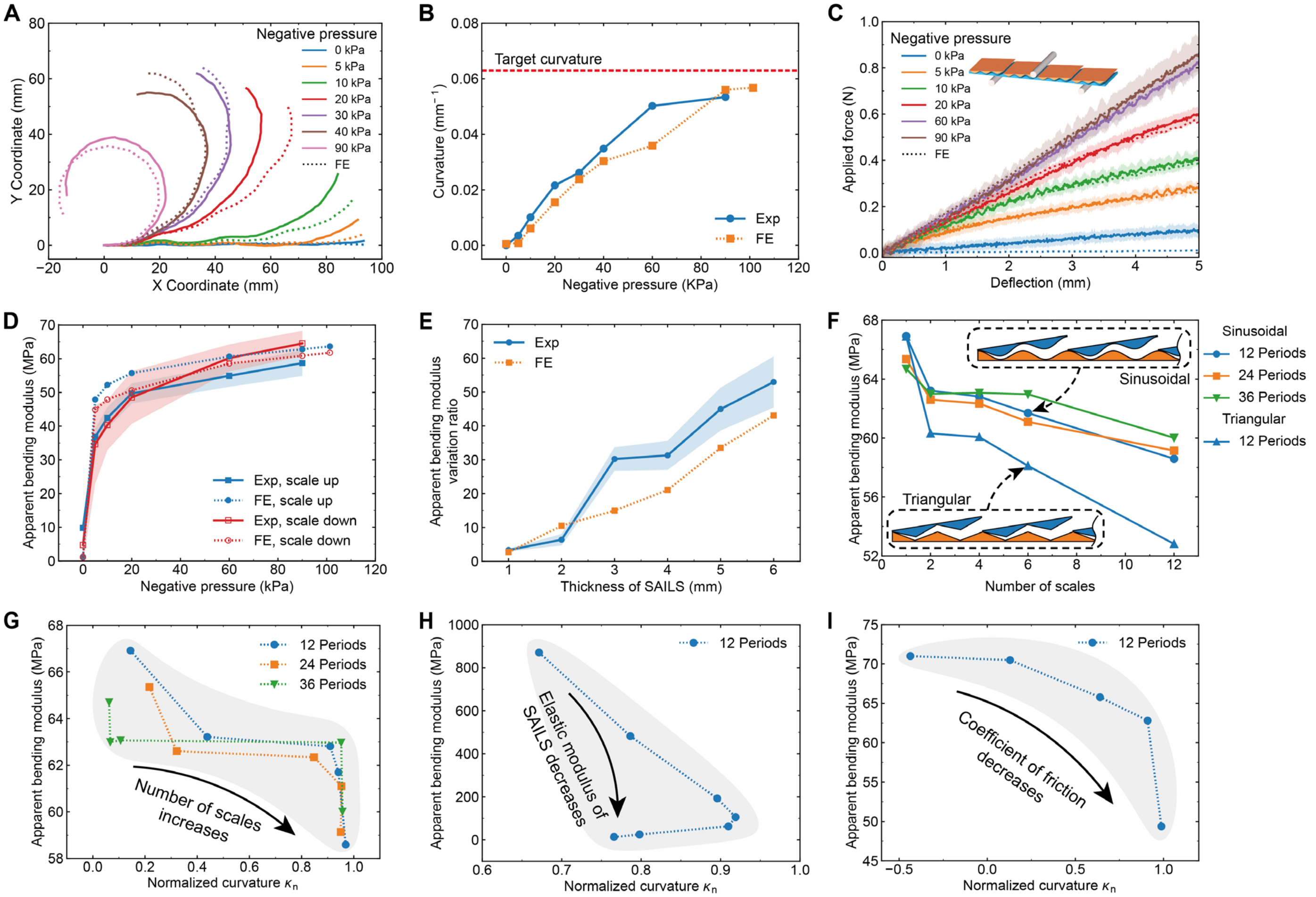

Fig. 3. Characterization of the shape-morphing and stiffness variation capabilities of SAILS. (**A**) Comparison of the actuated shape of a circle-shaped SAILS between experiments and FE simulations under different negative pressures ranging from 0 to 90 kPa. (**B**) Quantitative comparison of the curvatures extracted from (A) between the simulations and experiments. The target curvature is included for reference. (**C**) Force-deflection curves of SAILS from the three-point bending tests under different negative pressures ranging from 0 to 90 kPa. (**D**) Comparison of the apparent bending modulus of SAILS between scale-up and scale-down test positions under different negative pressures varying from 0 to 90 kPa. FE simulation results are also included. (**E**) Apparent bending modulus variation ratio of SAILS under 90-kPa negative pressure to no negative pressure, plotted as a function of SAILS thickness. The FE simulation results are included for comparison. (**F**) Variation of the apparent bending modulus as a function of the number of scales ranging from 1 to 12. Comparisons were made between different total numbers of periods and shapes of the surface pattern including a sinusoidal shape and a triangular shape. The trade-off between the normalized curvature and the apparent bending modulus of SAILS with (**G**) the number of scales increasing from 1 to 6, (**H**) the elastic modulus of SAILS ranging from 10 MPa to 1 GPa, and (**I**) the coefficient of friction between the scales and the base layer ranging from 0 to 1.

with increasing negative pressure. When the negative pressure was above 60 kPa, the whole structure was linear elastic within our deflection range. The yielding behavior in the curves with a negative pressure lower than 60 kPa was caused by the separation and sliding between the scales and base layer. The FE simulation results (dotted lines in Fig. 3C) were in agreement with these experimental results (see Materials and Methods for details of the FE simulation).

The apparent bending moduli of SAILS under various negative pressures were calculated and are summarized in Fig. 3D (see Materials and Methods for the calculation of the apparent bending modulus). The shaded areas represent the SDs. We compared the results between two distinct loading directions—scale-up and scale-down configurations. In the scale-up case, where the scales faced the indenting rod (Fig. 3C, inset), the scales were subjected to compression while the base layer was under tension. On the contrary, in the scale-down configuration, where the base layer faced the indenting rod, the stress state was reversed. It can be seen in Fig. 3D that for the scale-up configuration, as the negative pressure increased from 0 to 5 kPa, the apparent bending modulus of the structure exhibited a rapid increase from 9.8 to 36.8 MPa. Note that the lowest apparent bending modulus of SAILS is only slightly higher than that of the base layer only, which is 6.65 MPa. Moreover, when the negative pressure exceeded 20 kPa, this apparent bending modulus increase became much less pronounced and approached a plateau, ultimately reaching 58.7 MPa at a pressure of 90 kPa. This measurement showed that our SAILS has a high stiffness variation ratio of ~6 times. The results also demonstrated that the stiffnesses under both the scale-up and scale-down conditions were similar, indicating that SAILS could accommodate loading from both directions and maintain a good load-bearing capacity. Furthermore, the FE simulation results aligned closely with the experimental outcomes (Fig. 3D). We also showed in the FE simulations that when the negative pressure increased to the physical limit of one atmospheric pressure (101 kPa), both the curvature and apparent bending modulus of SAILS were only slightly higher than those under 90 kPa (Fig. 3, B and D), meaning that a 90-kPa negative pressure was high enough to fully engage the scales and the base layer.

The stiffness variation ratio can be tuned by changing the thickness of SAILS, which is illustrated in Fig. 3E, where we varied the thickness of SAILS from 1 to 6 mm. The results show that as the thickness of SAILS increases, the apparent bending modulus variation ratio notably increases, with a maximum ratio of 53 achieved at a SAILS thickness of 6 mm. When calculating the ratio in FE simulation, the lowest modulus for each thickness was calculated with a negative pressure of 0.5 kPa.

The effects of the number of scales and total periods on the apparent bending modulus of SAILS are demonstrated in Fig. 3F. All data points were obtained from FE simulations under a negative pressure of 90 kPa (see Materials and Methods for a description of the FE simulations). All the samples had a thickness of 2 mm and a width of 3 cm. We compared three different numbers of periods—12, 24, and 36—while keeping the total length of the sample fixed at 10 cm. For each number of periods, we tested samples with different numbers of scales, namely, 1, 2, 3, 4, 6, and 12. In addition, the effects of different surface pattern shapes, including sinusoidal and triangular shapes, were evaluated, as shown in the insets of Fig. 3E. The results indicated that as the number of scales increased, the apparent bending modulus decreased in all cases. This was because an increase in the number of scales increased the number of cuts in the structure, subsequently compromising the stiffness of SAILS. As the number of scales increased, the sinusoidal-shaped surface pattern exhibited a higher apparent bending modulus than the triangular-shaped surface pattern. The results also showed that the number of periods had a negligible effect on the apparent bending modulus of SAILS.

In general, the shape-changing and load-bearing capabilities of engineered morphing materials are mutually exclusive (*46*). Here, we demonstrated this trade-off in Fig. 3G, where each data point corresponds to a specific design of SAILS, characterized by the number of scales and the number of periods on each scale. Despite sharing the same configuration, each data point was obtained from the testing of two samples designed into different shapes: a flat sample for the apparent bending modulus assessment and a circular-shaped sample for evaluating the shape-morphing ability. All samples were consistent in overall dimensions with a thickness of 2 mm, a length of 10 cm, and a width of 3 cm. Considering the good agreement between our simulations and experiments shown in previous results, all the results in Fig. 3G were obtained through FE simulations under a negative pressure of 90 kPa. Here, we used a normalized parameter κ_n to characterize the shape-morphing cability, which could be expressed as follows

$$\kappa_n = 1 - \frac{|\kappa - \kappa_t|}{|\kappa + \kappa_t|} \quad (1)$$

where κ is the morphed curvature and κ_t is the target curvature, namely, 0.0628 mm^{-1}. As a result, κ_n approached 0 when κ and κ_t were far apart and approached 1 when the two values were close (a detailed explanation for the choice of this parameter is presented in Supplementary Discussions). The results showed that as the number of scales increased, the apparent bending modulus decreased, whereas the normalized parameter κ_n increased for all cases, as shown in Fig. 3G, demonstrating the trade-off between the two properties. A similar trade-off also appeared when the length of SAILS was changed to 15 cm (fig. S5) or by varying the elastic modulus (Fig. 3H) of SAILS, the coefficient of friction between the scales and the base layer (Fig. 3I), or the elastic modulus of the airbag (fig. S6).

Application as a soft amphibious robot

To demonstrate the functionality and adaptability of SAILS, we used it to build a soft amphibious robot. Inspired by the movement of eels and snakes, our robot used traveling wave locomotion. This traveling wave-based motion enabled the robot to navigate both on ground (*47*–*50*) and in water (*51*, *52*), therefore making our robot amphibious. The design of the soft amphibious robot is shown in Fig. 4A and fig. S7. The robot was composed of three segments (indicated by different colors in Fig. 4A). Each segment of the robot consisted of two chambers at opposite sides, with each chamber enclosing SAILS designed to morph to a target shape of a half circle (fig. S7B). Each chamber was connected to a soft tube and could be individually actuated. The fabrication details are described in Materials and Methods. When a chamber was actuated, it deformed to the target shape with little constraint from the unactuated chamber on the opposite side because of the inherent softness of SAILS. Consequently, by applying negative pressure to different chambers in one segment, it could bend in two directions (Fig. 4B).

The control system of the soft amphibious robot is shown in Fig. 4C and is detailed in Materials and Methods. First, we showed that the robot was able to crawl on ground, as illustrated in Fig. 4D and movie S4. The corresponding control signals for each segment are depicted in Fig. 4E. By sequentially actuating the two chambers in each segment, we induced each segment to bend upward and downward alternatively. Here, the actuation period for each segment, denoted by T (Fig. 4E), was set to 0.5 s. A time shift φ, which was set to $T/4$, was introduced between each segment (Fig. 4E), resulting in a wave-shaped movement across the entire body of the soft robot. We developed a kinetic model based on the curvature of each segment of the robot to predict its movement on ground, as depicted in Fig. 4F. The modeled results closely align with the experimental movements illustrated in Fig. 4D. The detailed description of the model is provided in Materials and Methods and Supplementary Methods. Then, we demonstrated the robot swimming in water in Fig. 4F and movie S4. The corresponding control signals are shown in fig. S8. Note that because of the different locomotion mechanisms, the actuation sequence of the three segments of the robot when swimming on water was opposite to that when crawling on ground, as shown in Fig. 4E and fig. S8.

We then showcased the multifunctionality and adaptability of the robot. The robot's ability to overcome an obstacle and transition from land to water is showcased in Fig. 5A and movie S5. First, the robot overcame a 10-mm-high obstacle. This was achieved by bending the first segment upward as the robot approached the obstacle, which allowed the robot to climb on top of the obstacle ($t = 7$ s), after which the robot resumed its wave-like locomotion to continue forward ($t = 29$ s). Then, the robot navigated a downward slope and entered the water tank. Once most of the robot was submerged ($t = 60$ s), the direction of the traveling wave was reversed, enabling the robot to swim forward in the water. In Fig. 5B and movie S6, we illustrated the adaptability of the robot by demonstrating its

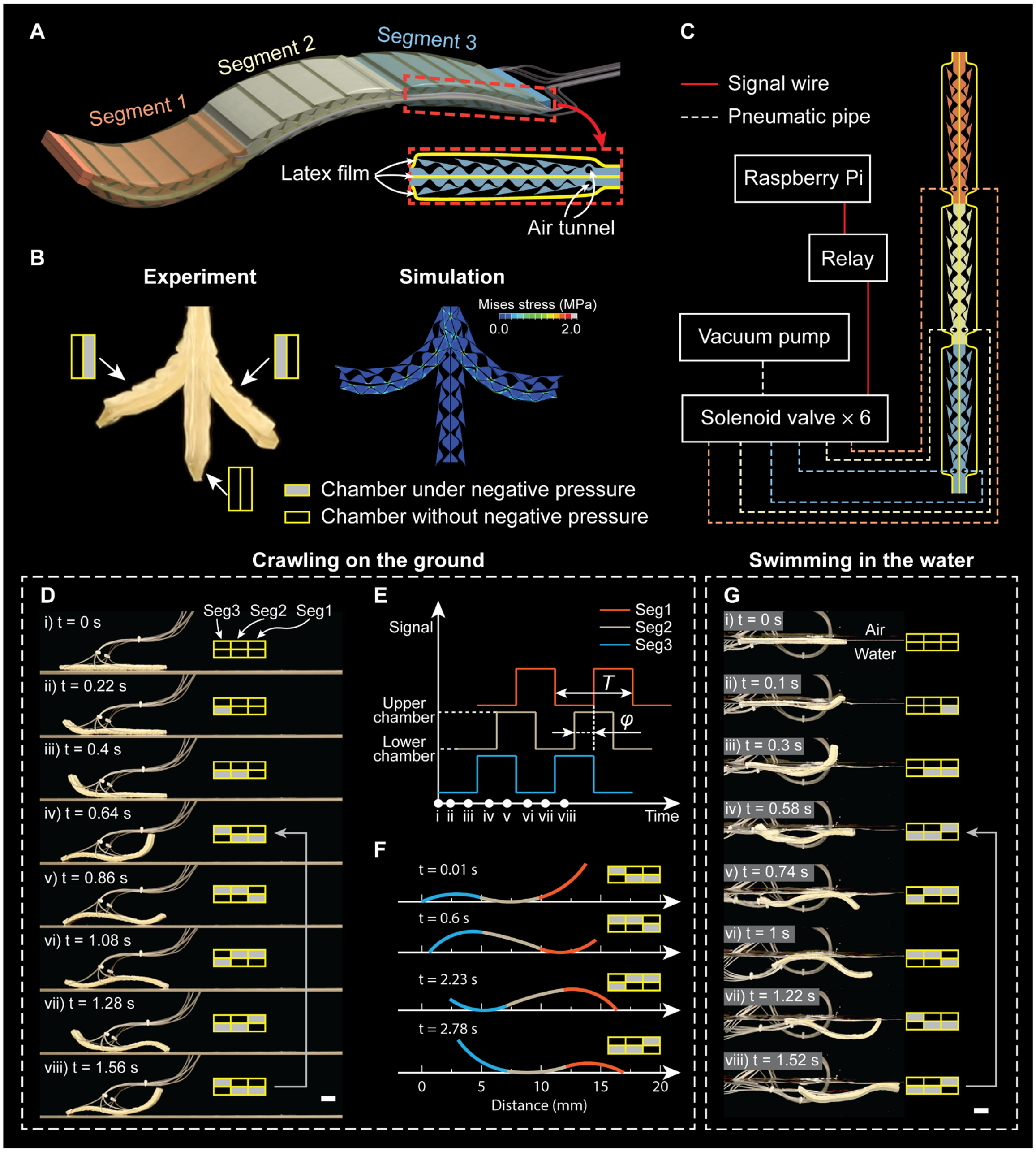

Fig. 4. The design, control, and characterization of the soft amphibious robot. (**A**) The design of the robot, which consists of three segments, each comprising two chambers. (**B**) Characterization of the bidirectional bending of one segment of the robot under a negative pressure of 90 kPa. The FE simulation is included for comparison. (**C**) The control system of the robot, comprising a Raspberry Pi, a six-channel relay, a vacuum pump, and six solenoid valves. (**D**) Sequential snapshots of the robot crawling on ground during its launch and the first control cycle. (**E**) The sequence of the control signal for the three segments of the robot as it crawls on ground. (**F**) Configurations of the robot predicted at four different time points based on the model. (**G**) The sequence of the control signal for the three segments of the robot as it swims in water. Scale bar, 2 cm.

capability to navigate through a series of restricted spaces with gap limits gradually decreasing from 20 to 8 mm. Owing to the inherent softness of the robot, it could adapt its shape to the restricted environment, albeit with a reduction in its speed. The load-carrying ability of the robot is demonstrated in Fig. 5C and movie S7. The load carried by the robot was 50 g, which was nearly twice the weight of the robot (27 g, without tube). In addition, as demonstrated in Fig. 5D and movie S7, the robot could climb a slope with a 22° incline.

We further studied the effect of the actuation frequency f, which was defined as $f = 1/T$, on the speed of the robot, as shown in Fig. 5E. The results showed that the robot had a higher speed in water than on ground. Moreover, the speed of the robot first increased and then decreased as the frequency *f* increased. This was because when *f* was low, the speed of the actuation wave traveling across the body of the robot was low, resulting in a low locomotion speed. However, when *f* was too high ($f > 4$ Hz), none of the robot segments could be fully actuated. As a result, the deformation of each segment was small, which also led to a low locomotion speed. Therefore, there existed an optimal actuation frequency ($f = 0.56$ Hz on ground and $f = 1.25$ Hz in water) for the speed of the robot. Using the kinetic model we developed, we can predict the speed of the robot crawling on ground at varying frequencies, as demonstrated in Fig. 5E. In addition, we formulated a dynamic model to predict the speed of the robot in water (see Materials and Methods for details). The predictions from the model align closely with our experimental results (Fig. 5E).

We summarized the speed of the robot under different scenarios in Fig. 5F, including on ground, in water, on a 22° slope, and with a 50-g load. The robot exhibited exceptional performance when swimming at the water surface, achieving a speed of 0.34 body lengths (BL) per second, much higher than the speeds obtained under the other conditions including on ground, on a slope, and while carrying a load.

To demonstrate the unique capabilities bestowed by the variable-stiffness characteristic of SAILS, we designed a larger robot, twice the thickness and width and approximately double the length of the one depicted in Figs. 4 and 5. In Fig. 6A and movie S8, we first illustrate the robot's ability to crawl over an obstacle (*t* = 100 s). Subsequently, we applied negative pressure to both chambers in the first and third segments and the upper chamber of the middle segment. This transformed the robot into a bridge (*t* = 127.8 s), allowing a toy car to pass over it (*t* = 130.5 s). Figure 6B and movie S8 further showcase its protective function by demonstrating the robot crawling over a quail egg (*t* = 83.7 s) and then deploying as a protective structure (*t* = 116 s) to shield the egg from a falling ball of 50 g. This was achieved by applying negative pressure to the upper chambers of all three segments. Without protection from the robot, the egg would be broken by the ball, as shown in the inset of Fig. 6B. Moreover, in movie S8, we show the enhanced load-carrying capability of the larger robot carrying a load of 1.26 kg, which is seven times its own weight (180 g).

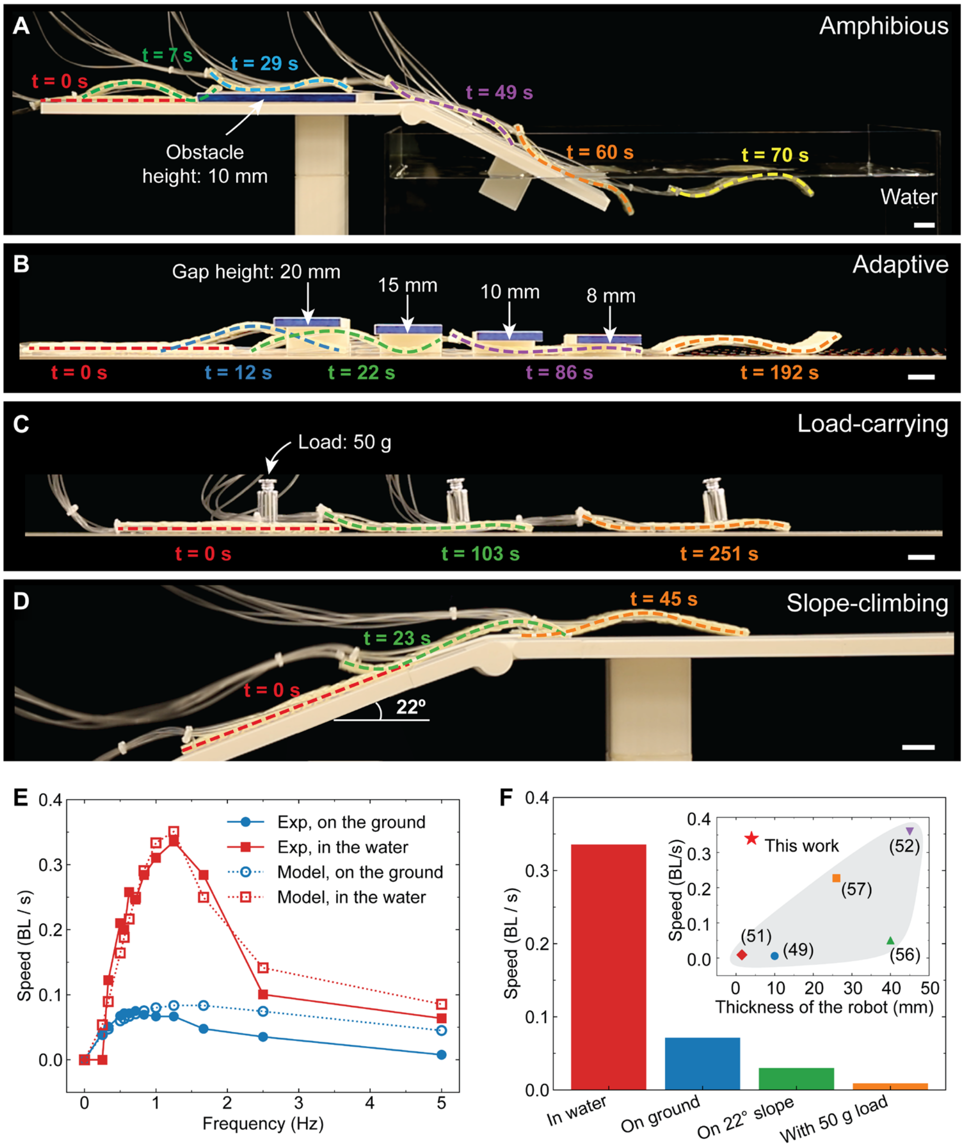

Fig. 5. The multifunctionality and speed characterization of the soft amphibious robot. (**A**) The robot overcoming an obstacle and transitioning from ground to water. (**B**) The robot navigating through a series of confined spaces with gap limits ranging from 20 to 8 mm. (**C**) The robot crawling while carrying a 50-g load. (**D**) The robot climbing a slope of 22°. (**E**) The speed of the robot under different actuation frequencies. (**F**) The speed of the robot under various locomotion scenarios, including in water, on ground, on a 22° slope, and when carrying a 50-g load. The inset compares the speed and thickness of this robot with those of other soft undulatory robots (*49*, *51*, *52*, *56*, *57*). Scale bar, 2 cm.

Application as an adaptive drone landing system

Various studies have shown that structures with variable stiffness are proficient candidates for energy absorption (*53*, *54*). Leveraging this insight, we developed a hook-shaped landing gear for drones using SAILS, as depicted in Fig. 7. The design of the landing gear is shown in fig. S9. To achieve an independent system on the drone, we added a vacuum pump, solenoid valves, a pressure gauge, and a Raspberry Pi to the drone to control the deployment of the landing gear. The fabrication and assembly details are described in Materials and Methods. To quantify the impact mitigation capability of this adaptive landing gear, we conducted a series of drop tests with the drone, releasing it from two heights: a lower altitude of 3 cm and a higher altitude of 20 cm, as illustrated in movie S9. The experimental setup is depicted in Fig. 7A. The experimental procedure is described in Materials and Methods. The recorded impact forces over time under the four negative pressures, 10, 20, 50, and 90 kPa, are presented in Fig. 7 (C and D). The results revealed an interesting phenomenon: At a lower drop height, the maximum impact force rose with increasing negative pressure, whereas at a higher drop height, the maximum impact force decreased with increasing negative pressure. These trends were captured quantitatively in Fig. 7E and aligned well with observations on other structures with tunable stiffness (*54*).

To explain this phenomenon, we conducted FE simulations on the compression of the landing gear under two different negative pressures: 10 and 90 kPa. The force-displacement curves, depicted in Fig. 7 (F and G), allow us to compare the energy absorption capacities, represented by the areas under the curves. The shaded regions beneath each pair of curves in Fig. 7 (F and G) are equal in area in their respective figures. The shaded areas in Fig. 7F represent a lower energy absorption than those in Fig. 7G, corresponding to the scenario where the drone is dropped from a lower height. In this case, because the landing gear under the negative pressure of 10 kPa has a lower stiffness, it has a lower peak force. Conversely, Fig. 7G shows that, under higher energy impacts (corresponding to the drone dropping from a higher altitude), the landing gear with under a lower negative pressure undergoes a pronounced increase in force. This is caused by the fixed end contacting the ground. On the contrary, the landing gear at 90 kPa did not collapse, leading to a lower peak force.

Using the onboard control system, we could specify the negative pressure applied to the landing gear, as shown in movie S10. We demonstrated the deployment process of the drone in Fig. 8A and movie S11, showing the landing gear deployed in the air ($t = 20.5$ s), followed by the drone successfully landing with the deployed landing gear ($t = 43.2$ s). Moreover, the landing gear can be used as a gripper to lift a load of 225 g, as shown in Fig. 8B and movie S12. We also showed in Fig. 8C that the drone can take off with the load. These demonstrations showed the versatility of SAILS as drone landing gear.

DISCUSSION

In this work, we introduced SAILS, an innovative structure that both mimics the natural scales of, for example, pangolins and integrates shape-morphing and variable-stiffness capabilities directly in a thin layered structure, using just one actuation input. SAILS was composed of a base layer and an array of scales affixed to it. When SAILS was sealed in an envelope and subjected to negative pressure, the programmed surface patterns on the scales and base layer coupled together, thereby changing the overall shape and stiffness of the structure. We showcased the shape-morphing ability of SAILS by designing several 1D surfaces with zero Gaussian curvature and 2D surfaces with nonzero Gaussian curvature. We also evaluated the stiffness of SAILS using three-point bending experiments, finding that a 2-mm-thick SAILS could achieve a fivefold increase in bending modulus when a negative pressure of 90 kPa was applied. Furthermore, the FE models we developed could accurately reproduce the three-point bending and shape-morphing results obtained from the experiments, providing a tool for us to design SAILS.

Compared with previously reported variable-stiffness mechanisms (*11*, *21*–*24*, *26*, *27*, *30*, *55*), the main advantage of SAILS is its capability to concurrently modify stiffness and shape with a single negative pressure input (see table S2). Although some structures present a higher stiffness variation ratio (*30*, *55*), they necessitate additional mechanisms for morphing, which adds to the system complexity. In

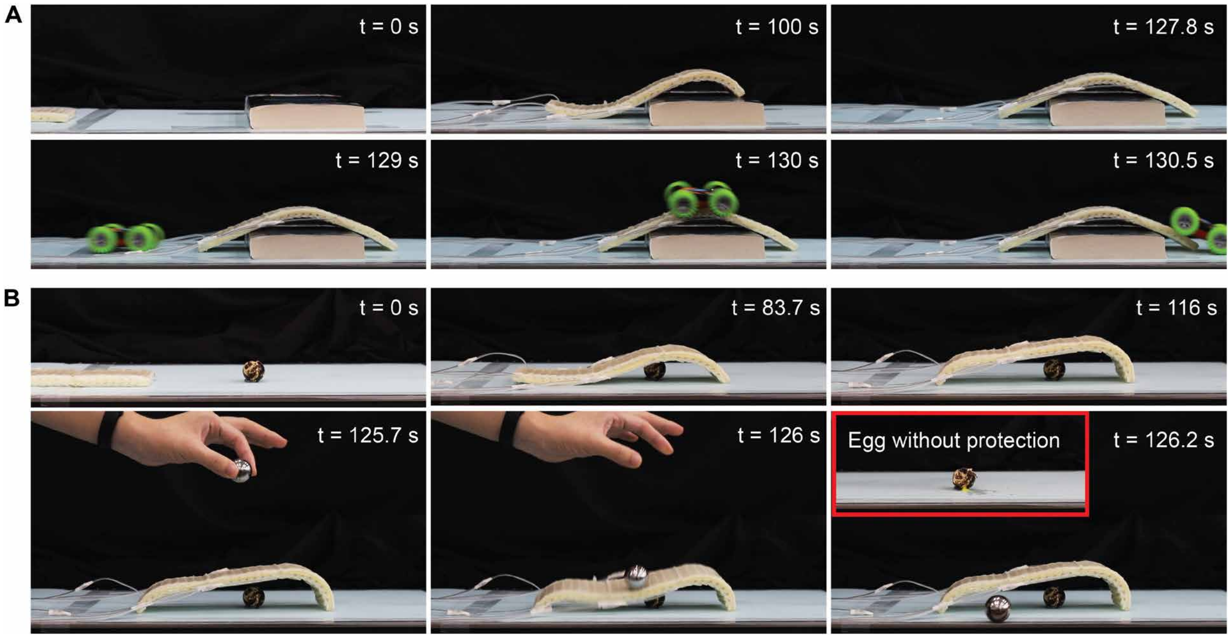

Fig. 6. Demonstration of the robot functioning as a bridge and protective structure. (**A**) The robot crawls over an obstacle and then transforms into a bridge, enabling a toy car to pass over it. (**B**) The robot crawls over a quail egg and subsequently deploys as a protective structure, shielding the egg from the impact of a falling ball of 50 g. In the absence of protection from the robot, the quail egg is broken by the ball.

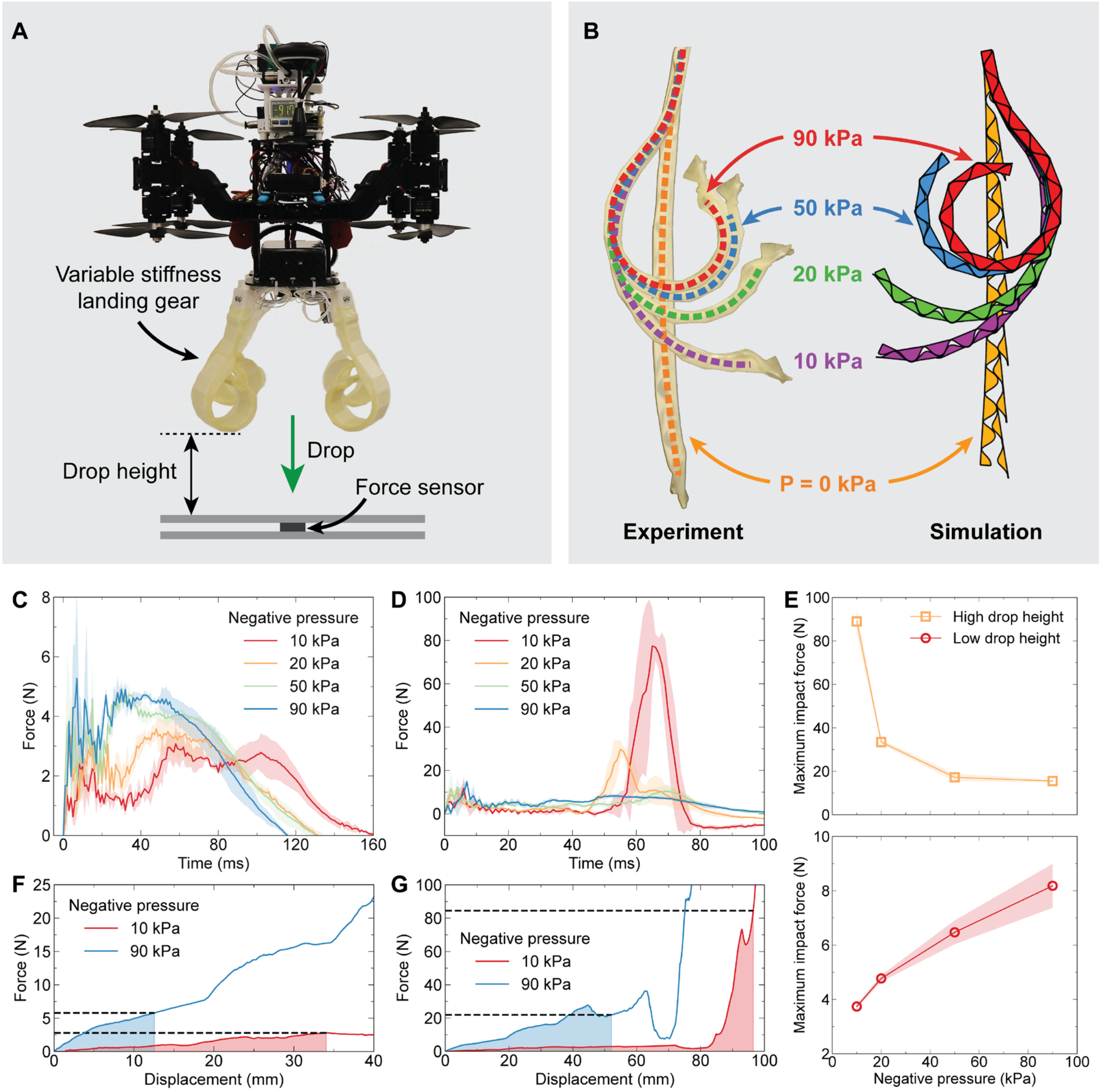

Fig. 7. The variable-stiffness landing gear for a drone. (**A**) The experimental setup for measuring the impact force of the drone. (**B**) The designed landing gear under five different negative pressures ranging from 0 to 90 kPa. The force-time curves recorded under four different negative pressures for the drone from a height of (**C**) 3 cm and (**D**) 20 cm. (**E**) The maximum impact force extracted from figures (C) and (D). Simulated force-displacement curves of the landing gear under compression for (**F**) low and (**G**) high levels of energy absorption.

the best case we have explored so far, SAILS achieved a stiffness variation ratio of 53, which is larger than many of the jamming-based systems that exhibit ratios ranging from 10 to 26 (*23*, *24*, *26*, *27*). We note that the thickness of SAILS is among the smallest in the jamming-based systems.

The relatively thin profile of SAILS, coupled with its integrated shape-morphing ability, endows it with a unique capacity to operate in confined spaces. Moreover, using negative pressure for actuation allows for a response time in seconds, notably quicker than osmotic-based (*11*) or heat-based (*21*, *22*) variable-stiffness actuators, which often respond in minutes or hours.

One limitation of the current SAILS design is its restriction to a single, predefined shape morphing. However, we have demonstrated that by integrating multiple SAILS segments, complex morphing behaviors are achievable. This is exemplified in our soft amphibious robot, which is able to complete a series of tasks including ground crawling, swimming, slope climbing, obstacle overcoming, and load bearing. We showed that the robot was adaptive, able to navigate through confined spaces with a gap height as low as 8 mm. Moreover, the robot could achieve a maximum speed of 0.34 BL/s when swimming and could be actuated at a high frequency of 5 Hz. Compared with soft undulatory robots (*49*, *51*, *52*, *56*, *57*), our robot combines a relatively high speed with a small thickness, as shown in the inset of Fig. 5F, which enables our robot to sustain efficient locomotion and navigate through confined spaces, a benefit derived from the compact design of SAILS. Currently, the robot is unable to move from water to another surface, which is a limitation we aim to address in future research.

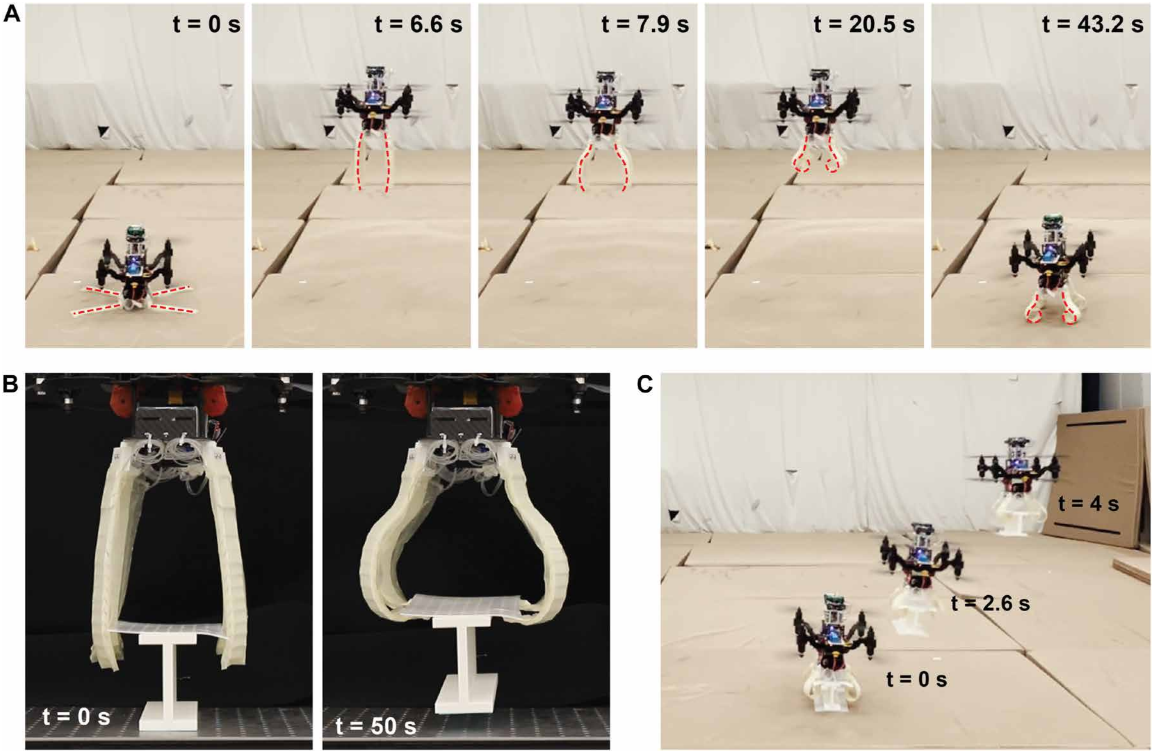

Fig. 8. Deployment process and load-carrying capability of drone adaptive landing gear. (**A**) Sequence showing drone takeoff, landing gear deployment, and landing. The red dashed lines indicate the landing gear. (**B**) The drone uses the landing gear as a gripper to lift a 225-g load. (**C**) The drone takes off carrying the load.

Furthermore, in potential applications such as medical devices and deployable structures, predictable and consistent actions often precede extensive shape variability. In these situations, the predefined morphing capabilities of SAILS may be adequate and beneficial. This is illustrated in our application of SAILS as a deployable drone landing gear. Unlike stationary shock absorbers that have a fixed response to impact, the key advantage of using SAILS as landing gear is its ability to adaptively change its stiffness, offering better protection against varying impact forces during landing. This is especially important for future drones to safely land on various terrains with different mechanical properties and with changing payloads and landing velocities. Moving forward, we are exploring ways to increase the morphing flexibility of SAILS, potentially through advanced control mechanisms or modular design approaches, to emulate the adaptability inherent in biological systems more closely.

Although the present SAILS demonstrates efficiency and versatility, it poses several challenges. Current pneumatic actuation necessitates tethering SAILS, and the connecting tube must maintain a certain radius to ensure adequate actuation speed. Using negative pressure as the sole actuation source presents an inherent physical limit. Factors like external loads can prevent the scales from being coupled with the base layer, causing SAILS to fail to achieve the designed shape or stiffness. In addition, our reliance on FDM fabrication means that different parts must be manually assembled. Implementing advanced manufacturing methods such as selective laser sintering would enable the integrated printing of SAILS, thus eliminating manual assembly (*24*). Furthermore, high-precision 3D printing techniques would allow for the creation of robots on a much smaller scale (*58*), making them apt for miniature and precise tasks. An additional limitation is the time-consuming nature of the FE simulations for SAILS. We will develop a more efficient model that can accurately and quickly predict the behavior of SAILS in future work.

Looking to the future, the implications of SAILS extend beyond its current applications. The principles demonstrated by SAILS can be leveraged to explore a generation of robots capable of unprecedented adaptability and multifunctionality. For instance, rescue robots designed using SAILS might exhibit greater versatility in navigating through debris or confined spaces, adjusting their stiffness and shape according to the encountered obstacles. Moreover, the potential to seamlessly transition between rigid and soft states suggests possible applications in surgical robots, where both gentle maneuvers and rigidity may be essential. With advances in manufacturing scalability and miniaturization, SAILS could also be integrated into wearable robotics, offering dynamic support and flexibility for individuals with mobility challenges. As the need for robots that can perform in unstructured environments grows, structures like SAILS will play a critical role in revolutionizing the capabilities and potentials of robotic platforms.

MATERIALS AND METHODS

Fabrication of SAILS

The scales and the base layer of SAILS were printed using a commercial FDM 3D printer (Raise3D Pro2, Raise3D Technologies Inc.) with a 95A TPU filament (3D Aura Pte Ltd.). To ensure the surface smoothness of the printed parts, we set the layer height to 0.02 mm in the slicing software ideaMaker. Before printing, the TPU filament was dried in a dry box at 70°C for 12 hours. After the parts were printed, a thin layer of PTFE tape (Taizhou Chenguang Plastic Industry Co. Ltd.) with a thickness of 0.05 mm was attached to the surfaces of both the scales and the base layer to reduce friction. The scales were then soldered onto the base layer using an electrical iron solder at 200°C. Then, the whole structure together with an air tube was sandwiched between two 0.1-mm-thick latex films (Shenzhen Dingzhi Rubber Products Co. Ltd.) and sealed using silicone glue (K-704 silicone adhesive, Guangdong Hengda New Materials Technology Co. Ltd.).

Three-point bending test of SAILS

The three-point bending test of SAILS was conducted on a universal testing machine (Mark-10 Corp) with a 25-N force sensor under displacement control. The loading speed was 0.1 mm/s, and the maximum deflection was 5 mm. An electropneumatic regulator (ITV2090-312 L5 regulator, SMC Corp.) was used to control the negative pressure of the scaled structure.

Calculation of the apparent bending modulus

The apparent bending modulus of SAILS was calculated using the following equation:

$$E = \frac{KL^3}{4bh^3} \tag{2}$$

where K is the slope of the initial linear part of the force-deflection curve in Fig. 3C and L is the distance between the two supporting rods in the three-point bending test. b and h are the width and thickness of SAILS, respectively. In the calculation of K, an initial 0.5-mm deflection was used for the cases with negative pressure ranging from 0 to 20 kPa, whereas an initial 2-mm deflection was used for the rest. This differentiation was made because of the extended elastic regime observed in the latter cases, as shown in Fig. 3C. Here, the values for L, b, and h were 7 cm, 3 cm, and 2 mm, respectively.

FE simulations

The FE simulations were conducted using Abaqus/Explicit (Dassault Systèmes Simulia Corp.). For the simulations of the structures with developable and nondevelopable surfaces shown in Fig. 2, the FE model was established in a 3D configuration. For the structures with developable surfaces, both SAILS and the airbag were modeled as deformable bodies using eight-node linear elements with reduced integration (C3D8R). Compared with the structures with nondevelopable surfaces, SAILS was modeled using six-node linear triangular prism elements with reduced integration (C3D6R). For the simulation of the three-point bending test and shape morphing shown in Fig. 3, the model was established in a 2D configuration under the plane strain condition to save computational time. SAILS and the airbag were simulated with four-node bilinear plane strain quadrilateral elements (CPE4), and the three rods were simulated as rigid bodies with two-node 2D linear rigid elements (R2D2). The configuration of the FE simulation of the three-point bending test is shown in fig. S10A. To ensure accuracy, the thinnest parts in the scales and the base layer in SAILS were modeled with four layers of element (see the right inset in fig. S10A). We also added bevels at the two ends of each scale so that the scales could slide over each other (see the left inset in fig. S10A). The negative pressure was applied to the outer surfaces of the airbag.

The TPU-printed SAILS was assumed to be linear elastic because the strain in the structure was small, with a maximum true strain of 0.26 (fig. S4). The elastic modulus of the printed TPU was set to be 55.7 MPa, which was obtained from the uniaxial tensile test. Poisson's ratio was set to be 0.48 to ensure a small material compressibility (*59*). The latex film was simulated using the neo-Hookean model (*60*). The uniaxial true stress-strain relation can be expressed as follows:

$$\sigma = \frac{E_{\text{latex}}}{3}[\exp(2\varepsilon) - \exp(-\varepsilon)] \tag{3}$$

where E_{latex} is the elastic modulus of latex. Here, E_{latex} was set to be 1.1 MPa, which was also obtained by fitting the uniaxial tensile test data. An inclined plane experiment was used to measure the friction coefficients between TPU, between TPU and latex, and between latex and steel supporting rods. The values obtained for these three friction coefficients were 0.13, 0.87, and 1, respectively.

Soft amphibious robot

We used a Raspberry Pi (4 Model B) to control a six-channel relay (G2RL-2, Shenzhen Biaokong Electric Technology Co. Ltd.), which connected to six solenoid valves (VK332V-5G-01, SMC Corp.), as shown in Fig. 4C. A vacuum pump (G4BL2490-2 T, Shanghai Pengpu Fluid Technology Co. Ltd.) was connected to the valves to provide a negative pressure of up to 90 kPa.

The assembly of the robot is shown in fig. S7A. We 3D-printed two layers, each having an end block and three SAILSs connected by three connectors. Every connector was attached to an air tube. Each SAILS had four scales each having two periods. After attaching the scales, the two printed layers were sandwiched between three latex films. We used silicone glue to seal the latex films and separate each chamber.

Modeling the speed of the soft amphibious robot on ground

For each segment of the robot, we modeled its shape as an arc, with its curvature being directly proportional to the applied negative pressure. The curvature values for each segment, from right to left, were denoted as κ_1, κ_2, and κ_3, respectively. We defined the curvature as positive when a segment bended upward and negative for downward bending. In a complete motion cycle, κ_3 was always the inverse of κ_1. The centers of the arcs corresponding to these three segments were determined using geometric relationships. Once these centers were established, we could obtain the full shape and position of the robot. We then calculated the forward displacement of the robot, which allowed us to compute the speed of the robot. A comprehensive description of this model is provided in Supplementary Methods.

Modeling the speed of the soft amphibious robot in water

The movement of the midline can be described as follows (*52*):

$$z = A\sin\left(\frac{2\pi}{\lambda}x - 2\pi ft\right) \tag{4}$$

where A is the amplitude, λ is the wavelength, and f is the motion frequency. For simplification, the water is assumed to be irrotational and incompressible. Under this assumption, the hydrodynamic forces resulting from the interaction between the water and the robot, including both the lift force F_L and the drag force F_D, are expressed as follows (*61*):

$$F_L = \frac{1}{2}\rho(c_{L1}\alpha + c_{L2}\alpha^2 + o(\alpha^2))v^2 S \tag{5}$$

$$F_D = \frac{1}{2}\rho(c_{D0} + c_{D1}\alpha + c_{D2}\alpha^2 + o(\alpha^2))v^2 S \tag{6}$$

where ρ is the water density, c_{Li} is the lift coefficient, c_{Di} is the drag coefficient, α is the angle of attack, v is the robot velocity, and S is the reference area. In addition, the added mass force caused by acceleration must be considered as follows:

$$F_A = \rho c_M a V \tag{7}$$

where $c_M = 1 + c_A$ is the inertia coefficient, c_A is the added mass coefficient, a is the robot acceleration, and V is the volume of the robot. Then, a can be calculated as follows:

$$a = \frac{\int_{x=0}^{l} (F_D^x |\cos(\theta_v)| - F_L^x |\sin(\theta_v)|) dx}{m - \rho c_M V} \tag{8}$$

where the superscript x represents the xth segment of the robot, θ_v is the angle between the velocity and the x axis, and m is the robot mass including the added mass effect. As for the unknown hydrodynamic coefficients, the mean absolute percentage error was used to find the optimal solution with the least deviation between the simulation and the experimental velocity.

Drone landing gear

Four identical 3D-printed drone landing gears were attached to an eight-propeller quadcopter (CQ360, Chengdu Lingjiang Technology Co. Ltd.) with 1-kg load-carrying ability. To achieve onboard control of the landing gear, we installed a Raspberry Pi Zero (2W), a pressure gauge (ZSE30A-01-C-L, SMC Corp.), a four-channel relay, a vacuum pump (G4BL1290-2 T, Shanghai Pengpu Fluid Technology Co. Ltd.), and a miniature solenoid valve (Dehnker Corp.) onto the drone. The components and the control diagram are shown in fig. S11.

A piezoelectric force sensor (Changzhou Arizon Technology Co. Ltd.) sandwiched between two aluminum plates was used to record the impact force during the impact test. A digital multimeter (Truevolt digital multimeter 34465A, Keysight Technologies Inc.) was used to record the voltage output of the piezoelectric force sensor. In the drop test, components for controlling the landing gear and the battery of the drone were not installed. The electropneumatic regulator (ITV2090-312 L5 regulator, SMC Corp.) was used to control the vacuum pressure applied to the landing gear.

Statistical analysis

For each case depicted in Fig. 3C, two samples were fabricated, and each was tested three times to determine the average force-deflection curves. The data from these tests were then used to calculate the average bending modulus in Fig. 3D. For Fig. 3E, one sample per case was fabricated and tested three times to calculate the average apparent bending modulus. The shaded areas in Fig. 3 (C to E) represent the SD.

The drop test of the drone was conducted three times for each experimental setup, namely, different dropping heights and negative pressures. The average curves and the SDs are plotted in Fig. 7 (C and D).

Supplementary Materials

This PDF file includes:

Methods
Discussions
Tables S1 and S2
Figs. S1 to S15

Other Supplementary Material for this manuscript includes the following:

Movies S1 to S12

REFERENCES AND NOTES

1. Y. Bar-Cohen, *Biomimetics: Biologically Inspired Technologies* (CRC Press, 2005).
2. S. Vogel, *Comparative Biomechanics: Life's Physical World* (Princeton Univ. Press, 2013).
3. S. Li, K. W. Wang, Plant-inspired adaptive structures and materials for morphing and actuation: A review. *Bioinspir. Biomim.* **12**, 011001 (2017).
4. W. M. Kier, K. K. Smith, Tongues, tentacles and trunks: The biomechanics of movement in muscular-hydrostats. *Zool. J. Linn. Soc.* **83**, 307–324 (1985).
5. D. Trivedi, C. D. Rahn, W. M. Kier, I. D. Walker, Soft robotics: Biological inspiration, state of the art, and future research. *Appl. Bionics Biomech.* **5**, 99–117 (2008).
6. C. Laschi, B. Mazzolai, M. Cianchetti, Soft robotics: Technologies and systems pushing the boundaries of robot abilities. *Sci. Robot.* **1**, eaah3690 (2016).
7. D. Rus, M. T. Tolley, Design, fabrication and control of soft robots. *Nature* **521**, 467–475 (2015).
8. J. Shintake, V. Cacucciolo, D. Floreano, H. Shea, Soft robotic grippers. *Adv. Mater.* **30**, e1707035 (2018).
9. M. Cianchetti, C. Laschi, A. Menciassi, P. Dario, Biomedical applications of soft robotics. *Nat. Rev. Mater.* **3**, 143–153 (2018).
10. X. Yang, Z. Wang, B. Zhang, T. Chen, C. Linghu, K. Wu, G. Wang, H. Wang, Y. Wang, Self-sensing robotic structures from architectured particle assemblies. *Adv. Intell. Syst.* **5**, 2200250 (2023).
11. I. Must, E. Sinibaldi, B. Mazzolai, A variable-stiffness tendril-like soft robot based on reversible osmotic actuation. *Nat. Commun.* **10**, 344 (2019).
12. P. Polygerinos, N. Correll, S. A. Morin, B. Mosadegh, C. D. Onal, K. Petersen, M. Cianchetti, M. T. Tolley, R. F. Shepherd, Soft robotics: Review of fluid-driven intrinsically soft devices; manufacturing, sensing, control, and applications in human-robot interaction. *Adv. Eng. Mater.* **19**, 1700016 (2017).
13. F. Ilievski, A. D. Mazzeo, R. F. Shepherd, X. Chen, G. M. Whitesides, Soft robotics for chemists. *Angew. Chem. Int. Ed. Engl.* **50**, 1890–1895 (2011).
14. B. Mosadegh, P. Polygerinos, C. Keplinger, S. Wennstedt, R. F. Shepherd, U. Gupta, J. Shim, K. Bertoldi, C. J. Walsh, G. M. Whitesides, Pneumatic networks for soft robotics that actuate rapidly. *Adv. Funct. Mater.* **24**, 2163–2170 (2014).
15. M. Manti, V. Cacucciolo, M. Cianchetti, Stiffening in soft robotics: A review of the state of the art. *IEEE Robot. Autom. Mag.* **23**, 93–106 (2016).
16. K. Singh, S. Gupta, Controlled actuation, adhesion, and stiffness in soft robots: A review. *J. Intell. Robot. Syst.* **106**, 59 (2022).
17. A. Stilli, H. A. Wurdemann, K. Althoefer, Shrinkable, stiffness-controllable soft manipulator based on a bio-inspired antagonistic actuation principle in *2014 IEEE/RSJ International Conference on Intelligent Robots and Systems* (IEEE, 2014), pp. 2476–2481.
18. S. P. M. Babu, A. Sadeghi, A. Mondini, B. Mazzolai, Antagonistic pneumatic actuators with variable stiffness for soft robotic applications in *2019 2nd IEEE International Conference on Soft Robotics (RoboSoft)* (IEEE, 2019), pp. 283–288.
19. K. Althoefer, Antagonistic actuation and stiffness control in soft inflatable robots. *Nat. Rev. Mater.* **3**, 76–77 (2018).
20. C. Majidi, R. J. Wood, Tunable elastic stiffness with microconfined magnetorheological domains at low magnetic field. *Appl. Phys. Lett.* **97**, 164104 (2010).
21. D. Hwang, E. J. Barron III, A. B. M. Haque, M. D. Bartlett, Shape morphing mechanical metamaterials through reversible plasticity. *Sci. Robot.* **7**, eabg2171 (2022).
22. J. Shintake, B. Schubert, S. Rosset, H. Shea, D. Floreano, Variable stiffness actuator for soft robotics using dielectric elastomer and low-melting-point alloy in *2015 IEEE/RSJ International Conference on Intelligent Robots and Systems (IROS)* (IEEE, 2015), pp. 1097–1102.
23. L. Arleo, L. Lorenzon, M. Cianchetti, Variable stiffness linear actuator based on differential drive fiber jamming. *IEEE Trans. Robot.* **39**, 4429–4442 (2023).
24. Y. Wang, L. Li, D. Hofmann, J. E. Andrade, C. Daraio, Structured fabrics with tunable mechanical properties. *Nature* **596**, 238–243 (2021).
25. Y. S. Narang, J. J. Vlassak, R. D. Howe, Mechanically versatile soft machines through laminar jamming. *Adv. Funct. Mater.* **28**, 1707136 (2018).
26. Y. Wei, Y. Chen, T. Ren, Q. Chen, C. Yan, Y. Yang, Y. Li, A novel, variable stiffness robotic gripper based on integrated soft actuating and particle jamming. *Soft Robot.* **3**, 134–143 (2016).
27. B. Yang, R. Baines, D. Shah, S. Patiballa, E. Thomas, M. Venkadesan, R. Kramer-Bottiglio, Reprogrammable soft actuation and shape-shifting via tensile jamming. *Sci. Adv.* **7**, eabh2073 (2021).

28. P. Jiang, Y. Yang, M. Z. Q. Chen, Y. Chen, A variable stiffness gripper based on differential drive particle jamming. *Bioinspir. Biomim.* **14**, 036009 (2019).
29. V. Wall, R. Deimel, O. Brock, Selective stiffening of soft actuators based on jamming in *2015 IEEE International Conference on Robotics and Automation (ICRA)* (IEEE, 2015), pp. 252–257.
30. M. Ibrahimi, L. Paterno, L. Ricotti, A. Menciassi, A layer jamming actuator for tunable stiffness and shape-changing devices. *Soft Robot.* **8**, 85–96 (2021).
31. X. Zeng, H.-J. Su, A high performance pneumatically actuated soft gripper based on layer jamming. *J. Mech. Robot.* **15**, 014501 (2022).
32. D. Cao, J. G. Martinez, E. S. Hara, E. W. H. Jager, Biohybrid variable-stiffness soft actuators that self-create bone. *Adv. Mater.* **34**, e2107345 (2022).
33. W. Wang, N.-G. Kim, H. Rodrigue, S.-H. Ahn, Modular assembly of soft deployable structures and robots. *Mater. Horiz.* **4**, 367–376 (2017).
34. P. Rawat, D. Zhu, M. Z. Rahman, F. Barthelat, Structural and mechanical properties of fish scales for the bio-inspired design of flexible body armors: A review. *Acta Biomater.* **121**, 41–67 (2021).
35. S. Dharmavaram, H. Ebrahimi, R. Ghosh, Coupled bend-twist mechanics of biomimetic scale substrate. *J. Mech. Phys. Solids* **159**, 104711 (2022).
36. M. S. Hossain, H. Ebrahimi, R. Ghosh, Fish scale inspired structures-A review of materials, manufacturing and models. *Bioinspir. Biomim.* **17**, 061001 (2022).
37. A. Shafiei, F. Barthelat, 3D mechanics of scaled membranes. *Int. J. Solids Struct.* **241**, 111498 (2022).
38. B. Wang, W. Yang, V. R. Sherman, M. A. Meyers, Pangolin armor: Overlapping, structure, and mechanical properties of the keratinous scales. *Acta Biomater.* **41**, 60–74 (2016).
39. J. Xu, C. Fu, Q. Fu, Y. Chen, Y. Ma, X. Feng, Flexible arc-armor inspired by origami. *Int. J. Mech. Sci.* **201**, 106463 (2021).
40. M. Connors, T. Yang, A. Hosny, Z. Deng, F. Yazdandoost, H. Massaadi, D. Eernisse, R. Mirzaeifar, M. N. Dean, J. C. Weaver, C. Ortiz, L. Li, Bioinspired design of flexible armor based on chiton scales. *Nat. Commun.* **10**, 5413 (2019).
41. S. Zuo, K. Iijima, T. Tokumiya, K. Masamune, Variable stiffness outer sheath with "Dragon skin" structure and negative pneumatic shape-locking mechanism. *Int. J. Comput. Assist. Radiol. Surg.* **9**, 857–865 (2014).
42. T. Sun, C. Yuanlong, H. Tianyu, J. Chenlei, L. Binbin, S. Yimin, A soft gripper with variable stiffness inspired by pangolin scales, toothed pneumatic actuator and autonomous controller. *ROBOT. CIM-INT. MANUF.* **61**, 101848 (2020).
43. Y. Bao, H. Liu, Z. Zhao, X. Ma, X.-Y. Zhang, G. Liu, W.-L. Song, Toward flexible embodied energy: Scale-inspired overlapping lithium-ion batteries with high-energy-density and variable stiffness. *Adv. Funct. Mater.* **33**, 2301581 (2023).
44. R. H. Soon, Z. Yin, M. A. Dogan, N. O. Dogan, M. E. Tiryaki, A. C. Karacakol, A. Aydin, P. Esmaeili-Dokht, M. Sitti, Pangolin-inspired untethered magnetic robot for on-demand biomedical heating applications. *Nat. Commun.* **14**, 3320 (2023).
45. C. Wang, Z. Lv, M. P. Mohan, Z. Cui, Z. Liu, Y. Jiang, J. Li, C. Wang, S. Pan, M. F. Karim, A. Q. Liu, X. Chen, Pangolin-inspired stretchable, microwave-invisible metascale. *Adv. Mater.* **33**, e2102131 (2021).
46. F. Hannard, M. Mirkhalaf, A. Ameri, F. Barthelat, Segmentations in fins enable large morphing amplitudes combined with high flexural stiffness for fish-inspired robotic materials. *Sci. Robot.* **6**, eabf9710 (2021).
47. X. Qi, H. Shi, T. Pinto, X. Tan, A novel pneumatic soft snake robot using traveling-wave locomotion in constrained environments. *IEEE Robot. Autom. Lett.* **5**, 1610–1617 (2020).
48. D. Zarrouk, M. Mann, N. Degani, T. Yehuda, N. Jarbi, A. Hess, Single actuator wave-like robot (SAW): Design, modeling, and experiments. *Bioinspir. Biomim.* **11**, 046004 (2016).
49. M. Watanabe, H. Tsukagoshi, Soft sheet actuator generating traveling waves inspired by gastropod's locomotion in 2017 *IEEE International Conference on Robotics and Automation (ICRA)* (IEEE, 2017), pp. 602–607.
50. M. M. Serrano, A. H. Chang, Z. Guangcong, P. A. Vela, Incorporating frictional anisotropy in the design of a robotic snake through the exploitation of scales in *2015 IEEE International Conference on Robotics and Automation (ICRA)* (IEEE, 2015), pp. 3729–3734.
51. C. Christianson, N. N. Goldberg, D. D. Deheyn, S. Cai, M. T. Tolley, Translucent soft robots driven by frameless fluid electrode dielectric elastomer actuators. *Sci. Robot.* **3**, eaat1893 (2018).
52. D. Q. Nguyen, V. A. Ho, Anguilliform swimming performance of an eel-inspired soft robot. *Soft Robot.* **9**, 425–439 (2022).
53. Y. S. Narang, A. Degirmenci, J. J. Vlassak, R. D. Howe, Transforming the dynamic response of robotic structures and systems through laminar jamming. *IEEE Robot. Autom. Lett.* **3**, 688–695 (2018).
54. Y. Wang, B. Ramirez, K. Carpenter, C. Naify, D. C. Hofmann, C. Daraio, Architected lattices with adaptive energy absorption. *Extreme Mech. Lett.* **33**, 100557 (2019).
55. Y. S. Narang, B. Aktaş, S. Ornellas, J. J. Vlassak, R. D. Howe, Lightweight highly tunable jamming-based composites. *Soft Robot.* **7**, 724–735 (2020).
56. E. Milana, B. Van Raemdonck, K. Cornelis, E. Dehaerne, J. De Clerck, Y. De Groof, T. De Vil, B. Gorissen, D. Reynaerts, EELWORM: A bioinspired multimodal amphibious soft robot in *2020 3rd IEEE International Conference on Soft Robotics (RoboSoft)* (IEEE, 2020), pp. 766–771.
57. H. Feng, Y. Sun, P. A. Todd, H. P. Lee, Body wave generation for anguilliform locomotion using a fiber-reinforced soft fluidic elastomer actuator array toward the development of the eel-inspired underwater soft robot. *Soft Robot.* **7**, 233–250 (2020).
58. S. R. Dabbagh, M. R. Sarabi, M. T. Birtek, S. Seyfi, M. Sitti, S. Tasoglu, 3D-printed microrobots from design to translation. *Nat. Commun.* **13**, 5875 (2022).
59. H. J. Qi, M. C. Boyce, Stress-strain behavior of thermoplastic polyurethanes. *Mech. Mater.* **37**, 817–839 (2005).
60. L. R. G. Treloar, Stresses and birefringence in rubber subjected to general homogeneous strain. *Proc. Phys. Soc.* **60**, 135–144 (1948).
61. W. Wang, X. Dai, L. Li, B. H. Gheneti, Y. Ding, J. Yu, G. Xie, Three-dimensional modeling of a fin-actuated robotic fish with multimodal swimming. *IEEE/ASME Trans. Mechatron.* **23**, 1641–1652 (2018).

Acknowledgments: We thank J. Xiao for help with the drone flight test. **Funding:** This work was supported by A*STAR Singapore through the RIE2025 MTC IRG Award M21K2c0118 and the RIE2020 AME YIRG Award A2084c0162. Y.W. acknowledges the NAP award 020482 from Nanyang Technological University Singapore. **Author contributions:** T.C. and Y.W. developed the overall concept, designed the experiments, and analyzed the data. T.C. conducted the experiments and the simulations. T.C., X.Y., and B.Z. took the videos of the soft amphibious robot and the drone landing gear. J.L. and J.P. developed the models for the soft amphibious robot. Y.W. supervised the project. T.C. and Y.W. wrote the manuscript and the supplementary document. All the authors contributed to the discussion, data analysis, and editing of the manuscript. **Competing interests:** The authors declare that they have no competing interests. **Data and materials availability:** All data are available in the main text or the Supplementary Materials and are available at https://doi.org/10.21979/N9/MTJUKK.

Submitted 25 September 2023
Accepted 13 June 2024
Published 17 July 2024
10.1126/scirobotics.adl0307

Science Robotics

Scale-inspired programmable robotic structures with concurrent shape morphing and stiffness variation

Tianyu Chen, Xudong Yang, Bojian Zhang, Junwei Li, Jie Pan, and Yifan Wang

Sci. Robot. **9** (92), eadl0307. DOI: 10.1126/scirobotics.adl0307

Editor's summary

Animals and plants have the ability to respond dynamically to their environments depending on the requirements for a specific task. Chen *et al.* have taken inspiration from the scales of pangolins to develop a soft robotic layered structure with capabilities of shape morphing and stiffness variability. The scale-inspired layered structure (SAILS) relies on negative pressure and a high frequency of actuation to morph into shapes and stiffnesses of interest. They demonstrate the potential of SAILS in the form of an amphibious robot capable of swimming and crawling, as well as a drone landing gear capable of varying its stiffness to minimize the impact of landing. —Amos Matsiko

Science Robotics (ISSN 2470-9476) is published by the American Association for the Advancement of Science. 1200 New York Avenue NW, Washington, DC 20005. The title *Science Robotics* is a registered trademark of AAAS.